CHEMISTRY OF MATERIALS
Article

Chem. Mater. **2011,** *23,* 285–292 285
DOI:10.1021/cm1030975

Structural Evolution of the $BiFeO_3$−$LaFeO_3$ System

Dmitriy A. Rusakov,[†,‡] Artem M. Abakumov,[§] Kazunari Yamaura,[‡] Alexei A. Belik,*[,†,‡] Gustaaf Van Tendeloo,[§] and Eiji Takayama-Muromachi[‡]

[†]*International Center for Materials Nanoarchitectonics (MANA), National Institute for Materials Science (NIMS), 1-1 Namiki, 1-1 Namiki, Tsukuba, Ibaraki 305-0044, Japan,* [‡]*National Institute for Materials Science (NIMS), 1-1 Namiki, Tsukuba, Ibaraki 305-0044, Japan, and* [§]*EMAT, University of Antwerp, Groenenborgerlaan 171, B-2020 Antwerp, Belgium*

Received October 27, 2010. Revised Manuscript Received December 5, 2010

The $(1 - x)BiFeO_3$−$xLaFeO_3$ system has been investigated and characterized by room-temperature and high-temperature laboratory and synchrotron powder X-ray diffraction, electron diffraction, high-resolution transmission electron microscopy, differential scanning calorimetry, and magnetization measurements. At room temperature, the ferroelectric *R*3*c* phase is observed for $0.0 \le x \le 0.10$. The $PbZrO_3$-related $\sqrt{2}a_p \times 2\sqrt{2}a_p \times 4a_p$ superstructure (where a_p is the parameter of the cubic perovskite subcell) is observed for $Bi_{0.82}La_{0.18}FeO_3$, while an incommensurately modulated phase is formed for $0.19 \le x \le 0.30$ with the $\sqrt{2}a_p \times 2a_p \times \sqrt{2}a_p$ basic unit cell. The $GdFeO_3$-type phase with space group *Pnma* ($\sqrt{2}a_p \times 2a_p \times \sqrt{2}a_p$) is stable at $0.50 \le x \le 1$. $Bi_{0.82}La_{0.18}FeO_3$ has no detectable homogeneity range (space group *Pnam*, $a = 5.6004(1)$ Å, $b = 11.2493(3)$ Å, $c = 15.6179(3)$ Å). The incommensurately modulated $Bi_{0.75}La_{0.25}FeO_3$ structure was solved from synchrotron X-ray powder diffraction data (*Imma*(00γ)*s*00 superspace group, $a = 5.5956(1)$ Å, $b = 7.8171(1)$ Å, $c = 5.62055(8)$ Å, $\mathbf{q} = 0.4855(4)\mathbf{c}^*$, $R_P = 0.023$, $R_{wP} = 0.033$). In this structure, cooperative displacements of the Bi and O atoms occur, which order within the (AO) (where A = Bi, La) layers, resulting in an antipolar structure. Local fluctuations of the intralayer antipolar ordering are compensated by an interaction with the neighboring (AO) layers. A coupling of the antipolar displacements with the cooperative tilting distortion of the perovskite octahedral framework is proposed as the origin of the incommensurability. All the phases transform to the $GdFeO_3$-type structure at high temperatures. $Bi_{0.82}La_{0.18}FeO_3$ shows an intermediate $PbZrO_3$-type phase with $\sqrt{2}a_p \times 2\sqrt{2}a_p \times 2a_p$ (space group *Pbam*; $a = 5.6154(2)$ Å, $b = 11.2710(4)$ Å, and $c = 7.8248(2)$ Å at 570 K). The compounds in the compositional range of $0.18 \le x \le 0.95$ are canted antiferromagnets.

1. Introduction

$BiFeO_3$ is a perovskite-type oxide crystallizing in space group *R*3*c* with $a = 5.579$ Å and $c = 13.869$ Å at room temperature (RT) and ambient pressure (AP). $BiFeO_3$ has received renewed and tremendous interest recently as a very rare example of a single-phase RT multiferroic.[1,2] In multiferroic systems, two (or all three) of the properties (anti)ferroelectricity, (anti)ferromagnetism, and ferroelasticity are observed simultaneously.[3,4] In $BiFeO_3$, the ferroelectric Curie temperature ($T_E = 1100$ K) and the antiferromagnetic Néel temperature ($T_N = 640$ K) are both well above RT,[2] and this compound continues to surprise with fascinating properties.[5−8]

Various chemical substitutions in $BiFeO_3$ have been investigated. Special attention has been paid to $Bi_{1-x}Ln_xFeO_3$ solid solutions (where Ln denotes rare-earth elements), because the magnetic B sublattice (of an ABO_3 perovskite) remains undisturbed in this case.[9−13] Bi^{3+} and La^{3+} ions have almost the same ionic radius.

*Author to whom all correspondence should be addressed. E-mail: Alexei.Belik@nims.go.jp.

(1) Wang, J.; Neaton, J. B.; Zheng, H.; Nagarajan, V.; Ogale, S. B.; Liu, B.; Viehland, D.; Vaithyanathan, V.; Schlom, D. G.; Waghmare, U. V.; Spaldin, N. A.; Rabe, K. M.; Wuttig, M.; Ramesh, R. *Science* **2003**, *299*, 1719.
(2) Catalan, G.; Scott, J. F. *Adv. Mater.* **2009**, *21*, 2463.
(3) Hill, N. A. *J. Phys. Chem. B* **2000**, *104*, 6694.
(4) Eerenstein, W.; Mathur, N. D.; Scott, J. F. *Nature* **2006**, *442*, 759.
(5) Choi, T.; Lee, S.; Choi, Y. J.; Kiryukhin, V.; Cheong, S.-W. *Science* **2009**, *324*, 63.
(6) Zeches, R. J.; Rossell, M. D.; Zhang, J. X.; Hatt, A. J.; He, Q.; Yang, C.-H.; Kumar, A.; Wang, C. H.; Melville, A.; Adamo, C.; Sheng, G.; Chu, Y.-H.; Ihlefeld, J. F.; Erni, R.; Ederer, C.; Gopalan, V.; Chen, L. Q; Schlom, D. G.; Spaldin, N. A.; Martin, L. W.; Ramesh, R. *Science* **2009**, *326*, 977.
(7) Wu, S. M.; Cybart, S. A.; Yu, P.; Rossell, M. D.; Zhang, J. X.; Ramesh, R.; Dynes, R. C. *Nat. Mater.* **2010**, *9*, 756.
(8) Kundys, B.; Viret, M.; Colson, D.; Kundys, D. O. *Nat. Mater.* **2010**, *9*, 803.
(9) Cheng, C.-J.; Kan, D.; Lim, S.-H.; McKenzie, W. R.; Munroe, P. R.; Salamanca-Riba, L. G.; Withers, R. L.; Takeuchi, I.; Nagarajan, V. *Phys. Rev. B* **2009**, *80*, 014109.
(10) Karimi, S.; Reaney, I. M.; Levin, I.; Sterianou, I. *Appl. Phys. Lett.* **2009**, *94*, 112903.
(11) Levin, I.; Karimi, S.; Provenzano, V.; Dennis, C. L.; Wu, H.; Comyn, T. P.; Stevenson, T. J.; Smith, R. I.; Reaney, I. M. *Phys. Rev. B* **2010**, *81*, 020103.
(12) Karimi, S.; Reaney, I. M.; Han, Y.; Pokorny, J.; Sterianou, I. *J. Mater. Sci.* **2009**, *44*, 5102.
(13) (a) Fujino, S.; Murakami, M.; Anbusathaiah, V.; Lim, S.-H.; Nagarajan, V.; Fennie, C. J.; Wuttig, M.; Salamanca-Riba, L.; Takeuchi, I. *Appl. Phys. Lett.* **2008**, *92*, 202904. (b) Kan, D.; Palova, L.; Anbusathaiah, V.; Cheng, C. J.; Fujino, S.; Nagarajan, V.; Rabe, K. M.; Takeuchi, I. *Adv. Funct. Mater.* **2010**, *20*, 1108. (c) Cheng, C. J.; Borisevich, A. Y.; Kan, D.; Takeuchi, I.; Nagarajan, V. *Chem. Mater.* **2010**, *22*, 2588.

Published on Web 12/23/2010

However, "the exact nature and even the number of structural phase transitions, as a function of La doping, is still an open question".[2] The earlier published data are controversial. Four structural variations in the $(1 - x)$-$BiFeO_3$−$xLaFeO_3$ system were reported without detailed symmetry assignment (the $R3c$ symmetry at $0 \le x \le 0.19$, a $PbZrO_3$-type phase at $0.20 \le x \le 0.55$, and two other phases with the boundary at $x = 0.75$).[14,15] A generally accepted picture includes six compositionally and crystallographically distinct phases with the $R3c$, $P1$, $C222$, $C222_1$, $Pn2_1a$, and $Pnma$ space symmetries with boundaries at $x = 0.06$, 0.24, 0.40, 0.55, and 0.7.[16−24] Unclear phase relationships in this system can be at the origin of the controversy in the reported properties. For example, ferroelectric properties were reported to survive up to $x = 0.2$,[25] $x = 0.4$,[18] or $x = 0.5$.[15]

Recent work on the $(1 - x)BiFeO_3$−$xLaFeO_3$ system has introduced even more controversy.[25−27] Either five ($R3c$, $P1$, $P4mm$, $P4/mmm$, $Pnma$)[25] or three ($R3c$, $Imma$, $Pnma$)[26,27] structural variations have been suggested. In this work, we performed an accurate and detailed investigation of the $(1 - x)BiFeO_3$−$xLaFeO_3$ system. We found four structural modifications: $R3c$, $Pnam$ ($PbZrO_3$-related with $\sqrt{2}a_p \times 2\sqrt{2}a_p \times 4a_p$), an incommensurately modulated phase with $\sqrt{2}a_p \times 2a_p \times \sqrt{2}a_p$ and the $Imma(00\gamma)s00$ superspace group, and $Pnma$ ($GdFeO_3$-type with $\sqrt{2}a_p \times 2a_p \times \sqrt{2}a_p$). We suggest that the discrepancy in the literature is caused by the lack of thermodynamic equilibrium and by the presence of the ferroelectric $R3c$ and canted antiferromagnetic $Pnma$ ($GdFeO_3$-type) end members in many of the previous works.

2. Experimental Section

2.1. Synthesis of $(1 - x)BiFeO_3$−$xLaFeO_3$. Samples were synthesized from stoichiometric mixtures of Bi_2O_3 (99.9999%), Fe_2O_3 (99.999%), and La_2O_3 (99.9%). La_2O_3 was annealed at 1270 K before use. Initial mixed powders were pressed into pellets and annealed at different conditions (which are specified below for each composition) on platinum plates. One pellet of each composition was used to prevent direct contact between the platinum plate and the remaining part of the sample, because of a possible reaction between platinum and Bi_2O_3.[2] The heating and cooling time was 4 h for each annealing temperature. The annealing time at each temperature was 12 h (if not specified). The final annealing temperature will be given below. The samples were reground after each annealing step and pelletized before further annealing.

2.2. Characterization of $(1 - x)BiFeO_3$−$xLaFeO_3$. Powder X-ray diffraction (XRD) data were collected at room temperature on a Rigaku Model Ultima III diffractometer, using Cu $K\alpha$ radiation (for a 2θ range of 5°−100°, a step width of 0.02°, and a counting time of 2−10 s/step). Room-temperature (RT) and high-temperature (HT) synchrotron powder X-ray diffraction (SXRD) data were collected on a large Debye−Scherrer camera at the BL02B2 beamline[28] of SPring-8 from 290 K to 950 K. HT SXRD data were collected for 5 min at each temperature point, with a heating time of 1−2 min from one temperature point to the next one. The incident beam from a bending magnet was monochromatized to $\lambda = 0.41905$ Å. The samples were contained in (boro)glass and quartz capillary tubes with an inner diameter of 0.2 mm, and the capillary tubes were rotated during measurements. The SXRD data were collected in a 2θ range from 2° to 75° with a step interval of 0.01° (the data from 2° to 50° were used in the refinements). Diffraction data were analyzed by the Rietveld method with Rietan-2000[29] and Jana2006.[30]

Magnetic measurements were performed on a SQUID magnetometer (Quantum Design, MPMS) between 2 K and 400 K in an applied field of 1 kOe under both zero-field-cooled (ZFC) and field-cooled (FC; on cooling) conditions. Isothermal magnetization measurements were performed between −50 kOe and 50 kOe at 5 K and 300 K.

Differential scanning calorimetry (DSC) curves were recorded on a Mettler Toledo DSC1 STAR^e system at a heating/cooling rate of 10 K/min under N_2 flow from 293 K to 970 K in open platinum capsules.

Electron diffraction (ED) and high-resolution transmission electron microscopy (HRTEM) investigations were performed on crushed samples deposited on holey carbon grids. ED patterns and energy-dispersive X-ray (EDX) spectra were obtained using a Tecnai G2 microscope equipped with an energy-dispersive X-ray analysis (EDAX) attachment. HRTEM experiments were performed using the Tecnai G2 microscope operated at 200 kV and a Titan G3 electron microscope equipped with an aberration image corrector operated at 300 kV. HRTEM image simulations were made using the JEMS software.

3. Results

3.1. The *R3c* Phase. The $R3c$ phase was found in the Bi-rich samples of the $Bi_{1-x}La_xFeO_3$ system ($x \approx 0$−0.5) after annealing under the following conditions: 870 °C (12 h) + 910 °C (12 h) + 910 °C (12 h). However, a single $R3c$ phase was obtained only for $x = 0.05$ and $x = 0.1$.

(14) Roginskaya, Yu. E.; Venevtsev, Yu. N.; Fedotov, S. A.; Zhdanov, G. S. *Sov. Phys. Crystallogr.* **1964**, *8*, 490.
(15) Polomska, M.; Kaczmarek, W.; Pajak, Z. *Phys. Status Solidi* **1974**, *23*, 567.
(16) Gabbasova, Z. V.; Kuz'min, M. D.; Zvezdin, A. K.; Dubenko, I. S.; Murashov, V. A.; Rakov, D. N.; Krynetsky, I. B. *Phys. Lett. A* **1991**, *158*, 491.
(17) (a) Yuan, G. L.; Baba-Kishi, K. Z.; Liu, J.-M.; Or, S. W.; Wang, Y. P.; Liu, Z. G. *J. Am. Ceram. Soc.* **2006**, *89*, 3136. (b) Jiang, Q.-H.; Nan, C.-W.; Shen, Z.-J. *J. Am. Ceram. Soc.* **2006**, *89*, 2123.
(18) Zhang, S. T.; Pang, L. H.; Zhang, Y.; Lu, M. H.; Chen, Y. F. *J. Appl. Phys.* **2006**, *100*, 114108.
(19) Chen, J. R.; Wang, W. L.; Li, J.-B.; Rao, G. H. *J. Alloys Compd.* **2008**, *459*, 66.
(20) Gonzalez Garcia, F.; Riccardi, C. S.; Simxes, A. Z. *J. Alloys Compd.* **2010**, *501*, 25.
(21) Simoes, A. Z.; Garcia, F. G.; Riccardi, C. S. *Mater. Chem. Phys.* **2009**, *116*, 305.
(22) Le Bras, G.; Colson, D.; Forget, A.; Genand-Riondet, N.; Tourbot, R.; Bonville, P. *Phys. Rev. B* **2009**, *80*, 134417.
(23) Lin, Yu.-H.; Jiang, Q.; Wang, Y.; Nan, C.-W. *Appl. Phys. Lett.* **2007**, *90*, 172507.
(24) Sahu, J. R.; Rao, C. N. R. *Solid State Sci.* **2007**, *9*, 950.
(25) Yuan, G. L.; Or., S. W.; Chan, H. L. W. *J. Phys. D: Appl. Phys.* **2007**, *40*, 1196.
(26) Troyanchuk, I. O.; Bushinsky, M. V.; Karpinskii, D. V.; Mantytskaya, O. S.; Fedotova, V. V.; Prokhnenko, O. I. *JETP Lett.* **2008**, *87*, 641.
(27) Troyanchuk, I. O.; Bushinsky, M. V.; Karpinskii, D. V.; Mantytskaya, O. S.; Fedotova, V. V.; Prokhnenko, O. I. *Phys. Status Solidi B* **2009**, *246*, 1901.
(28) Nishibori, E.; Takata, M.; Kato, K.; Sakata, M.; Kubota, Y.; Aoyagi, S.; Kuroiwa, Y.; Yamakata, M.; Ikeda, N. *Nucl. Instrum. Methods Phys. Res., Sect. A* **2001**, *467−468*, 1045.
(29) Izumi, F.; Ikeda, T. *Mater. Sci. Forum* **2000**, *321−324*, 198.
(30) Petricek, V.; Dusek, M. *The Crystallographic Computing System JANA2000*; Institute of Physics: Praha, Czech Republic, 2000.

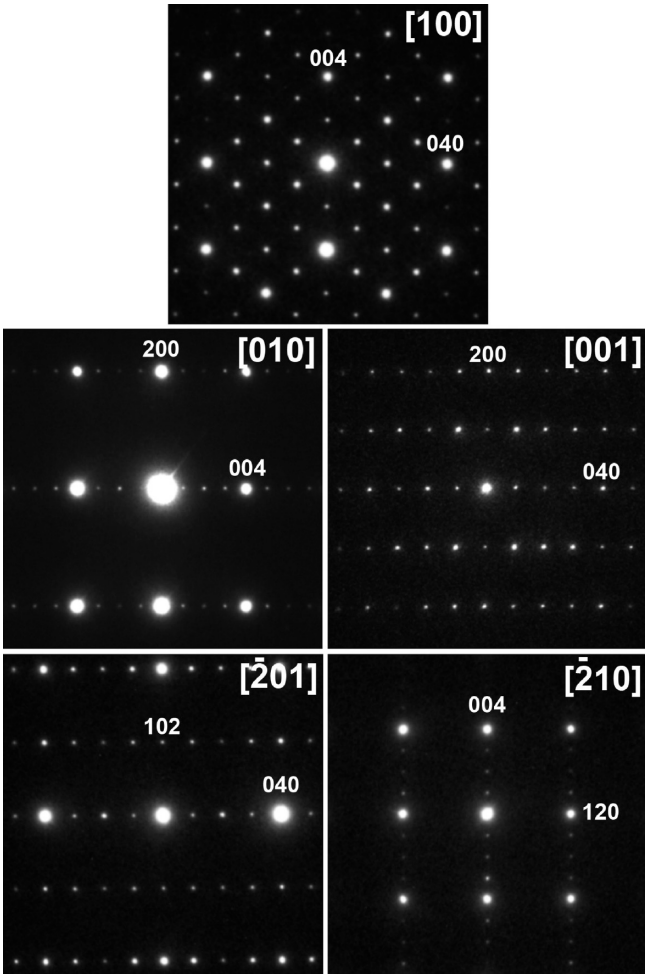

Figure 1. Electron diffraction patterns of the *Pnam* $PbZrO_3$-related phase in the $Bi_{0.85}La_{0.15}FeO_3$ (1025 °C) sample.

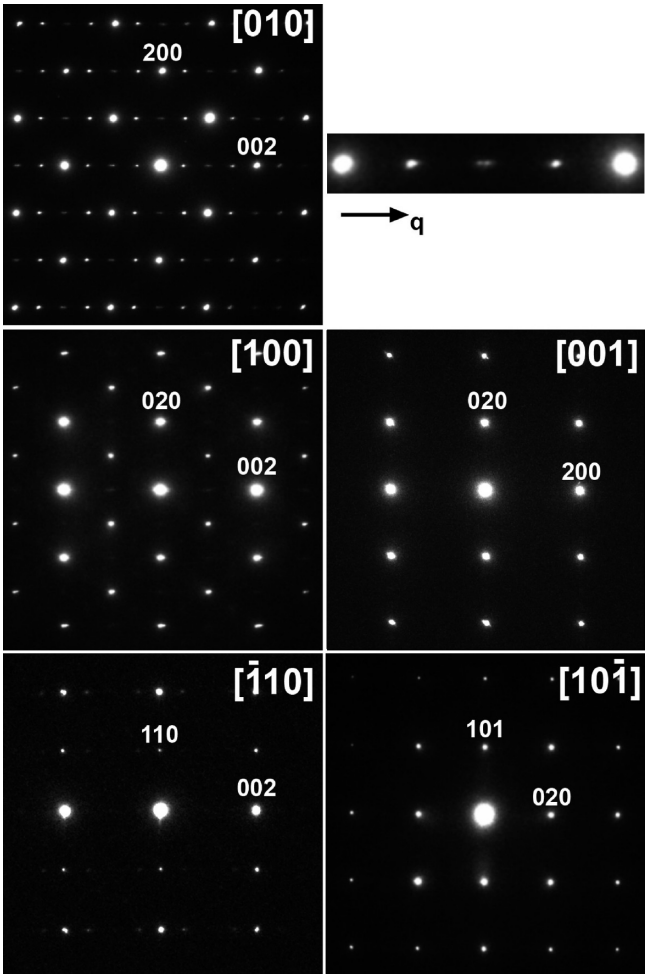

Figure 2. Electron diffraction patterns of the incommensurately modulated (IM) $Bi_{0.75}La_{0.25}FeO_3$ (1075 °C) phase. The enlarged portion of the [010] ED pattern demonstrates nonoverlapping second-order satellites.

Other samples were mixtures of three phases: *R*3*c*, $PbZrO_3$-related phases, and *Pnma* $GdFeO_3$-type phase (see Figure S1 of the Supporting Information). The existence of three perovskite phases in the quasi-binary $BiFeO_3-LaFeO_3$ system indicates that the phase equilibrium has not been reached. The *R*3*c* phase is stable in the $x = 0.1$ sample up to 1000 °C and partially decomposes at 1025 °C, releasing Fe_2O_3 and Bi_2O_3. The lattice parameters of the *R*3*c* phase in $Bi_{0.9}La_{0.1}FeO_3$ are $a = 5.5778(1)$ Å and $c = 13.8066(3)$ Å. The *R*3*c* phase disappears in the samples with $x \geq 0.18$ with further annealing at higher temperatures.

3.2. The *Pnam* $PbZrO_3$-Type Phase. A mixture of the *R*3*c* phase and the *Pnam* phase with the $PbZrO_3$-type structure was observed at $x = 0.15$ and 0.17 samples annealed at 1025 °C. This indicates a two-phase region between these phases. A pure *Pnam* phase was obtained at 1025 °C for $x = 0.18$ only ($a = \sqrt{2}a_p = 5.6004(1)$, $b = 2\sqrt{2}a_p = 11.2493(3)$, $c = 4a_p = 15.6179(4)$Å (a_p is the parameter of the perovskite subcell)). The lattice parameters and space symmetry of the *Pnam* phase were confirmed by electron diffraction. The ED patterns of the *Pnam* phase are shown in Figure 1. They can be indexed in an orthorhombic unit cell with the lattice parameters as determined from powder XRD. The reflection conditions $0kl$ ($k + l = 2n$) and $h0l$ ($h = 2n$) are in agreement with the space group *Pnam* or its acentric subgroup $Pna2_1$. The average chemical composition of the $x = 0.15$ sample determined by the EDX analysis was Bi:La:Fe = 41.8(1.5):8.7(6):49.5(1.4) (the expected composition is 42.5:7.5:50).

3.3. The Incommensurately Modulated (IM) Phase. The IM phase appears as a single phase in the $x = 0.19$ sample at 1025 °C. Its compositional range expands up to $x = 0.3$, when the annealing temperature is increased to 1075 °C. The ED patterns of the $x = 0.25$ sample confirm the formation of an incommensurately modulated structure (see Figure 2). The basic spots can be indexed on a body-centered orthorhombic unit cell with $a = \sqrt{2}a_p$, $b = 2a_p$, $c = \sqrt{2}a_p$. Arrays of satellite reflections, clearly visible on the [010] ED pattern (see Figure 2), are associated with each basic spot. The incommensurate position of the satellites is highlighted in the enlarged part of the [010] ED pattern, where the satellites corresponding to $\mathbf{H} + 2\mathbf{q}$ and $\mathbf{H} - 2\mathbf{q}$ (where $\mathbf{H}$ is the reciprocal vector of the basic spot, and $\mathbf{q}$ is the modulation vector) do not coincide. The indexation can be performed with the (3 + 1)-dimensional approach with a diffraction vector $\mathbf{h} = h\mathbf{a}^* + k\mathbf{b}^* + l\mathbf{c}^* + m\mathbf{q}$, $\mathbf{q} \approx 0.48\mathbf{c}^*$. Besides the reflection condition imposed by the body-centered lattice, the $0klm$ ($m = 2n$) reflection

Table 1. Selected Parameters from the Rietveld Refinement for $Bi_{0.75}La_{0.25}FeO_3$

formula	$Bi_{0.75}La_{0.25}FeO_3$
space group	*Imma*(00γ)*s*00
a	5.5977(1) Å
b	7.8172(1) Å
c	5.62061(8) Å
q	0.4855(4)**c***
unit cell volume, *V*	245.861(9) $Å^3$
calculated density	7.975 g/cm^3
radiation	synchrotron X-ray, λ = 0.41905 Å
2θ range	$3.5° \le 2\theta \le 52.5°$
2θ step	0.01°
R_P	0.023
R_{wP}	0.033
goodness of fit, GOF	2.52
R_F	
all reflections	0.029
main reflections	0.028
first-order satellites	0.030

condition is evident from the [100] ED pattern. The *hk*0 ($h,k \neq 2n$) reflections were often observed on the [001] ED pattern, because of twinning with the [100] ED pattern. Single-domain [001] ED patterns can be occasionally found without the *hk*0 ($h,k \neq 2n$) reflections. This suggests the superspace group *Imma*(00γ)*s*00. The powder XRD pattern of the IM phase ($x = 0.25$) was indexed using the ED data resulting in $a = 5.5977(1)$ Å, $b = 7.8172(1)$ Å, $c = 5.62061(8)$ Å, $\mathbf{q} = 0.4855(4)\mathbf{c}^*$. The EDX analysis of the $x = 0.25$ sample provided the Bi:La:Fe = 40(2):13(2):48(2) composition (the expected one is 37.5:12.5:50). The γ-component of the modulation vector slightly decreases as the La content increases (from $\gamma = 0.4899(4)$ for $x = 0.19$ to $\gamma = 0.4739(7)$ for $x = 0.28$) and monotonically decreases as the temperature increases, to $\gamma = 0.4765(4)$ for $x = 0.25$ at 670 K.

3.4. The *Pnma* $GdFeO_3$-Type Phase. A two-phase region between the IM and *Pnma* phases was observed for $x = 0.35-0.45$ at 1075 °C. Single-phase *Pnma* samples were obtained for $0.50 \le x \le 0.95$ at 1160 °C (1 h). The compositional dependence of the lattice parameters of the *Pnma* phase and the unit-cell volume for the entire system is given in Figure S2 of the Supporting Information.

3.5. Crystal Structure of the Incommensurately Modulated $Bi_{0.75}La_{0.25}FeO_3$ phase. The atomic coordinates of the $Bi_{0.55}La_{0.45}FeO_3$ (space group *Imma*)[27] structure were used as a starting model for the average structure. A random distribution of Bi^{3+} and La^{3+} ($^3/_4Bi^{3+}$ and $^1/_4La^{3+}$) over the A-position was assumed. The refinement of the atomic coordinates and atomic displacement parameters (ADPs) in the isotropic approximation resulted in poor reliability factors ($R_F = 0.131$, $R_P = 0.059$). The ADPs of the Bi/La, O1, and O2 atoms were unusually high (> 0.035 $Å^2$). Shifting the Bi/La atom and O1 atom from the 4*e* to 8*i* position by random displacement from the m_x mirror plane decreases the ADPs for these atoms and the reliability factors decrease to $R_F = 0.086$, $R_P = 0.047$. Therefore, the average model gives a poor description of the structure, but it does indicate that the modulation is probably related to atomic displacements of the A-cations and the oxygen atoms along the *a*-axis ($\{110\}_p$ direction).

Table 2. Atomic Positions, Atomic Displacement Parameters (ADPs), and Modulation Parameters for $Bi_{0.75}La_{0.25}FeO_3$[a]

atom	x_1	x_2	x_3	x_4^0	Δ	U_{iso} ($Å^2$)
Bi[b]	0.0505(4)	$^1/_4$	−0.0072(2)	0.283(3)	$^1/_2$	0.0117(3)
$U_{x,1} = 0.004(1)$, $U_{z,1} = 0.0054(5)$						
La[c]	0	0.267(1)	−0.0072(2)			0.016(3)
Fe	$^1/_2$	0	0			0.0098(3)
$A_{x,1} = 0.0059(7)$						
O(1)	0.433(2)	$^1/_4$	0.067(1)	0.316(3)	$^1/_2$	0.012(3)
O(2)	$^1/_4$	−0.0386(7)	$^1/_4$			0.017(2)
$A_{x,1} = -0.035(2)$, $A_{z,1} = -0.024(3)$						

[a] Modulation functions for the Bi atom for the parameter λ, defined in a restricted interval, are given by the following: $U_\lambda(x_4) = \sum_{n=0}^{k} U_{\lambda,n}\,\mathrm{ortho}_n(x_4)$, where the orthogonalized functions, obtained through a Schmidt orthogonalization routine, are given by $\mathrm{ortho}_0(x_4) = 1$ and $\mathrm{ortho}_1(x_4) = -1.890 + 3.024\sin(2\pi x_4)$. [b] g(Bi) = 0.75. [c] g(La) = 0.125.

In the *Imma*(00γ)*s*00, the m_x mirror plane shifts the modulation phase by $^1/_2$. Being applied to the $x_1, ^1/_4, x_3, x_4$ position of the Bi and O1 atoms, it transforms it to $-x_1, ^1/_4, x_3, ^1/_2+x_4$. Assigning a steplike occupational modulation with $\Delta = ^1/_2$ for the Bi and O1 position allows one to model the ordered arrangement of the atoms shifted either to the positive or negative direction along the *a*-axis: with $\Delta = ^1/_2$, the atoms with opposite displacement directions never coexist at the same place of the three-dimensional (3D) structure. One can assume that the displacement occurs because of the localization of the lone pair on the Bi^{3+} cation requiring strong short covalent bonds to some oxygen atoms, which would be the O1 atom. It suggests that the displacements of Bi and O1 should be conjugated to keep a short Bi−O1 interatomic distance (i.e., these atoms should always belong to the same *t*-section of the (3 + 1)D space, $t(Bi) = t(O1)$). The x_4^0 coordinates of the centers of their occupational domains then are related as $x_4^0(O1) = x_4^0(Bi) - \gamma z(Bi) + \gamma z(O1)$. However, the x_4^0 coordinate for these atoms is not fixed by symmetry. We found the refined x_4^0 value to be slightly larger than $^1/_4$ ($x_4^0 \approx 0.28$; see below and Table 2). This value, together with the γ-component of the modulation vector, defines the exact positions of the occupational domains. A more-detailed explanation of the symmetry relationships between the occupational domains and the resulting polar and antipolar structures is provided in Figures S3−S7 in the Supporting Information.

The derived arrangement of the occupational domains was used as input for the refinement. The Bi and La atoms that jointly occupy the A-position should be treated separately. Indeed, if, for the Bi^{3+} cations, the driving force for the polar displacement is obvious, such force is absent for the La^{3+} cations. The refinement of the anisotropic ADP for the La atom revealed that the U_{11} component is the smallest one, whereas the U_{22} component is the largest, indicating possible random displacement along the *b*-axis. The x_2 coordinate of the La atom was shifted from $^1/_4$ and the ADP was refined in the isotropic approximation. Since only the first-order satellites were observed, only corresponding harmonics were taken into account. For the Bi atom, they were taken in the orthogonolized form. The coefficients of the modulation functions, which were comparable to their standard

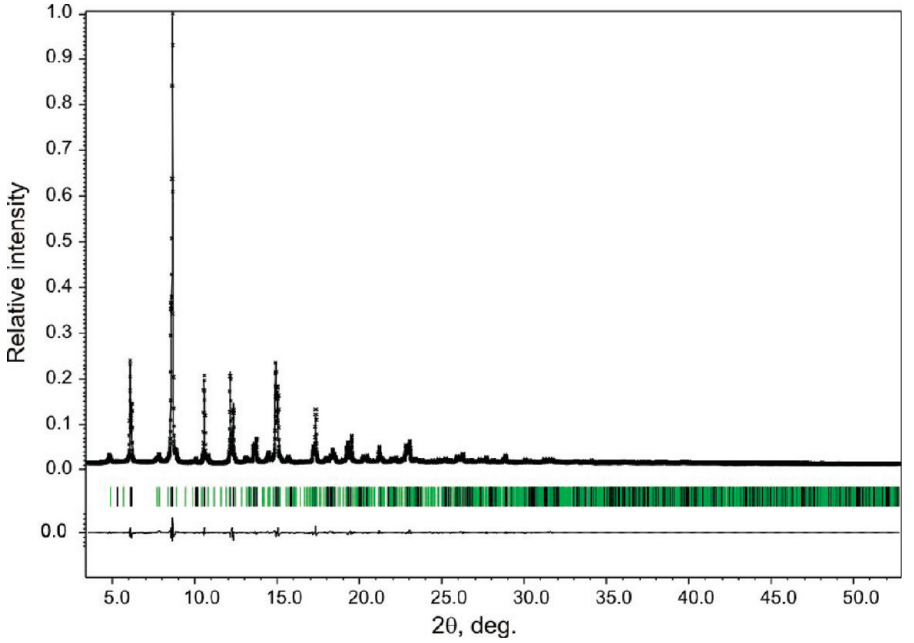

Figure 3. Experimental, calculated, and difference synchrotron powder X-ray diffraction (SXRD) profiles for $Bi_{0.75}La_{0.25}FeO_3$.

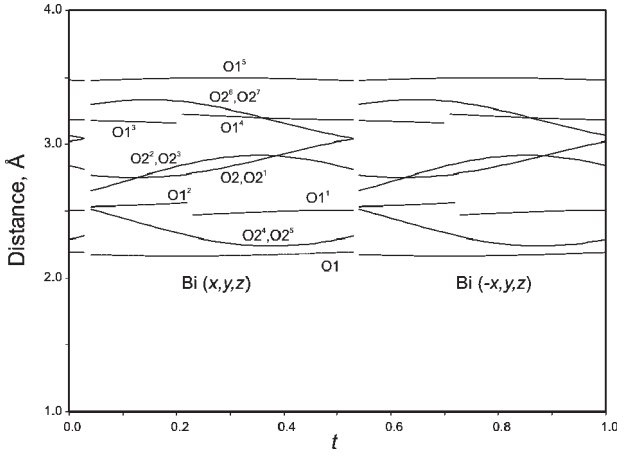

Figure 4. Interatomic Bi−O distances versus internal coordinate t ($t = x_4 - \mathbf{qr}_{av}$) in $Bi_{0.75}La_{0.25}FeO_3$. Symmetry codes are given in Table 3.

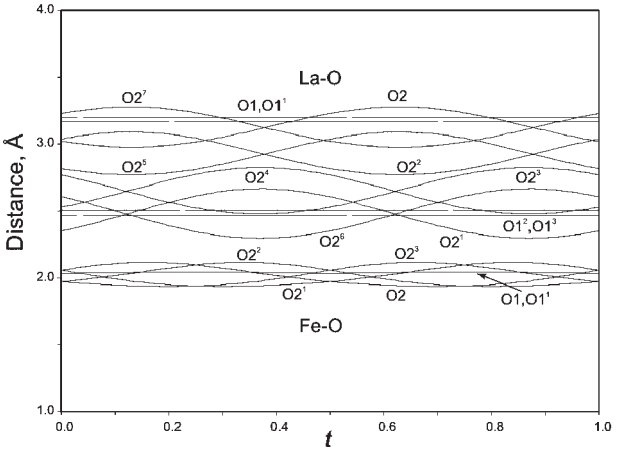

Figure 5. Interatomic La−O and Fe−O distances versus internal coordinate t ($t = x_4 - \mathbf{qr}_{av}$) in $Bi_{0.75}La_{0.25}FeO_3$. Symmetry codes are given in Table 3.

deviations, were set to zero. Selected crystallographic data and reliability factors for $Bi_{0.75}La_{0.25}FeO_3$ are provided in Table 1. Atomic positions, ADPs, and modulation parameters are listed in Table 2. Experimental, calculated, and difference SXRD profiles are shown in Figure 3. Interatomic distances, as a function of the internal coordinate t ($t = x_4 - \mathbf{qr}_{av}$), are shown in Figures 4 and 5 and are listed in Table 3.

3.6. HRTEM Investigation. The [$\bar{2}$10] HRTEM image of a well-ordered crystallite of the *Pnam* phase is shown in Figure 6. This orientation corresponds to the projection of the structure along the $\{001\}_p$ direction. The $c = 4a_p$ superstructure is visible on the image as brighter rows of the most prominent dots repeating every four perovskite unit cells. The presence of this superstructure is confirmed by a Fourier transform (inset), showing clear superlattice reflections.

The [010] HRTEM image of the IM phase is shown in Figure 7. Under these imaging conditions, the brighter dots correspond to a low projected potential (columns of the oxygen atoms and the places where the Bi and Fe columns are shifted apart). The modulation is seen as a variable brightness of the most prominent dots, particularly visible on the right part of the image. The image, calculated from a commensurate approximant of the IM structure (focus $f = -15$ nm, thickness $t = 1.6$ nm) is in excellent agreement with the experimental image.

3.7. Phase Transitions in $(1 - x)BiFeO_3 - xLaFeO_3$. The DSC data showed two anomalies for samples with $0.18 \leq x \leq 0.30$: one weak anomaly near 670−675 K (on heating) for all of the samples, because of an antiferromagnetic−paramagnetic phase transition[14,15] and the second stronger anomaly due to the structural phase transition to the *Pnma* $GdFeO_3$-type phase (centered at 777 K for $x = 0.18$, at 755 K for $x = 0.20$, at 682 K for $x = 0.25$, at 610 K for $x = 0.30$ on heating) (see Figure S8 of the Supporting Information). The second anomaly on the

Table 3. Main Interatomic Distances and Bond-Valence Parameters for $Bi_{0.75}La_{0.25}FeO_3$

distance	Main Interatomic Distance (Å)		
	average	min	max
Bi1−O1 (x,y,z)	2.18(2)	2.16(2)	2.227(16)
Bi1−O1[1] ($-x+{}^1/_2,y,-z+{}^1/_2$)	2.500(9)	2.494(9)	2.506(9)
Bi1−O1[2] ($x-{}^1/_2,-y+{}^1/_2,-z+{}^1/_2$)	2.535(10)	2.515(10)	2.555(11)
Bi1−O1[3] ($-x+{}^1/_2,y,-z-{}^1/_2$)	3.175(9)	3.157(9)	3.193(9)
Bi1−O1[4] ($x-{}^1/_2,-y+{}^1/_2,-z-{}^1/_2$)	3.190(10)	3.184(10)	3.200(10)
Bi1−O1[5] ($-x,y,z$)	3.48(2)	3.440(16)	3.50(2)
Bi1−O2 (x,y,z)			
Bi1−O2[1] ($-x+{}^1/_2,-y+{}^1/_2,-z+{}^1/_2$)	2.865(9)	2.749(10)	3.032(8)
Bi1−O2[2] ($x-{}^1/_2,y+{}^1/_2,z-{}^1/_2$)			
Bi1−O2[3] ($-x,-y,-z$)	2.834(13)	2.720(9)	2.901(17)
Bi1−O2[4] ($-x+{}^1/_2,-y,z-{}^1/_2$)			
Bi1−O2[5] ($x,y+{}^1/_2,-z$)	2.321(10)	2.243(11)	2.466(8)
Bi1−O2[6] ($-x,-y+{}^1/_2,z$)			
Bi1−O2[7] ($x-{}^1/_2,y,-z+{}^1/_2$)	3.218(12)	3.040(9)	3.324(15)
BVS(Bi)	2.92(5)	2.71(4)	3.12(6)
La1−O1 (x,y,z)			
La1−O1[1] ($-x,-y+{}^1/_2,z$)	2.465(10)	2.465(10)	2.465(10)
La1−O1[2] ($-x+{}^1/_2,y,-z+{}^1/_2$),			
La1−O1[3] ($x-{}^1/_2,-y+{}^1/_2,-z+{}^1/_2$)	2.505(8)	2.505(8)	2.505(8)
La1−O2 (x,y,z)	3.116(9)	2.980(11)	3.275(11)
La1−O2[1] ($x-{}^1/_2,y+{}^1/_2,z-{}^1/_2$)	2.467(8)	2.299(11)	2.662(11)
La1−O2[2] ($-x,-y+{}^1/_2,z$)	2.938(9)	2.773(11)	3.088(11)
La1−O2[3] ($-x+{}^1/_2,-y,z-{}^1/_2$)	2.660(8)	2.482(11)	2.821(11)
La1−O2[4] ($-x,-y,-z$)	2.638(8)	2.482(11)	2.822(11)
La1−O2[5] ($-x+{}^1/_2,-y+{}^1/_2,-z+{}^1/_2$)	2.918(9)	2.773(11)	3.088(11)
La1−O2[6] ($x,y+{}^1/_2,-z$)	2.490(8)	2.299(11)	2.662(11)
La1−O2[7] ($x-{}^1/_2,y,-z+{}^1/_2$)	3.135(9)	2.980(11)	3.275(11)
BVS(La)	2.93(3)	2.87(2)	2.99(3)
Fe1−O1 (x,y,z)			
Fe1−O1[1] ($x,-y,-z$)	2.029(3)	2.025(2)	2.031(3)
Fe1−O2 (x,y,z)			
Fe1−O2[1] ($-x,-y,-z$)	2.016(7)	1.960(11)	2.078(10)
Fe1−O2[2] ($-x+{}^1/_2,-y,z-{}^1/_2$)			
Fe1−O2[3] ($x+{}^1/_2,y,-z+{}^1/_2$)	2.011(7)	1.960(11)	2.078(10)
BVS(Fe)	3.00(2)	3.00(2)	3.01(2)

DSC curves becomes broader as the La content increases. The phase transition to the *Pnma* $GdFeO_3$-type phase was also confirmed by HT SXRD data measured for the *Pnam* ($x = 0.18$) (Figure 8a) and IM ($x = 0.25$) (Figure 8b) phases. In the $x = 0.18$ sample, weak superlattice reflections corresponding to the $c = 4a_p$ superstructure disappear at ~570 K, and the intermediate $PbZrO_3$-type $\sqrt{2}a_p \times 2\sqrt{2}a_p \times 2a_p$ *Pbam* structure is formed. The refined lattice parameters at 570 K are $a = 5.6154(2)$, $b = 11.2710(4)$, $c = 7.8248(2)$Å. Note that superlattice reflections corresponding to the $c = 4a_p$ were clearly observed for the *Pnam* phases at room temperature on both laboratory (see Figure S1 of the Supporting Information) and synchrotron XRD patterns (see Figure 8a), in contrast to $Bi_{0.85}Nd_{0.15}FeO_3$.[11] At 860 K, the reflections from the *Pnma* ($GdFeO_3$-type) phase appear in the $x = 0.18$ sample. Note that no DSC anomaly has been detected in $Bi_{0.82}La_{0.18}FeO_3$ corresponding to the *Pnam*−*Pbam* phase transition, probably because the structural changes are very small. The IM phase is stable up to ~620 K. Reflections corresponding to the *Pnma* ($GdFeO_3$-type) phase appear from 670 K (Figure 8a). A coexistence of both phases is observed up to 860 K, indicating a first-order phase transition. The lattice parameters of the *Pnma* $GdFeO_3$-type phase of $Bi_{0.75}La_{0.25}FeO_3$ at 950 K are $a = 5.6201(1)$ Å, $b = 7.9238(1)$ Å, $c = 5.5763(1)$ Å, and the refined structural parameters and temperature dependences of the lattice parameters are given in Table S1 and Figure S9 in the Supporting Information.

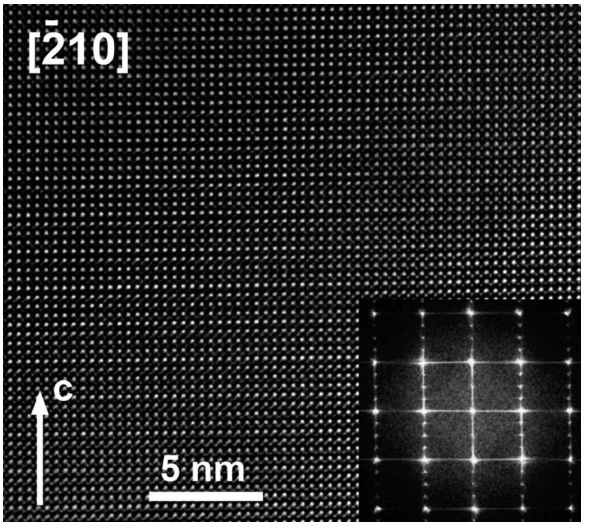

Figure 6. [$\bar{2}$10] HRTEM image of the *Pnam* $PbZrO_3$-type phase. The Fourier transform is shown as an inset.

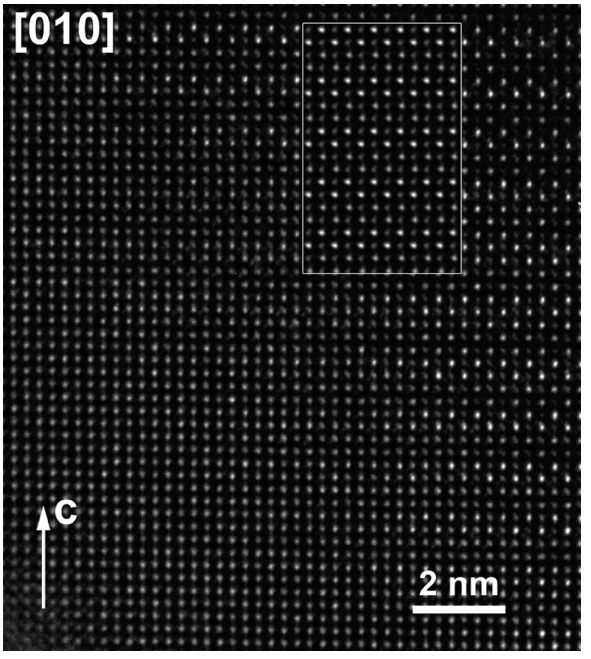

Figure 7. [010] HRTEM image of the IM phase. The calculated image (focus $f = -15$ nm, thickness $t = 1.6$ nm) is outlined by a white border.

3.8. Magnetic Properties. Temperature-dependent magnetization measurements for $Bi_{1-x}La_xFeO_3$ (x = 0.2, 0.25, 0.3, 0.35, and 0.4) revealed no anomalies below 400 K (see Figure S10 in the Supporting Information). Field-dependent magnetization measurements for the samples with $0.18 \leq x \leq 0.95$ showed well-defined hysteresis loops at 5 K and 300 K, which is typical for canted antiferromagnets (see Figure S11 in the Supporting Information).

4. Discussion

Using a combination of diffraction techniques, we have established the existence of four distinct phases in the

$(1-x)BiFeO_3-xLaFeO_3$ system. The ferroelectric $R3c$ phase is stable at $0.0 \le x \le 0.10$. A two-phase region ($0.15 \le x \le 0.17$) separates the $R3c$ phase from the $Bi_{0.82}La_{0.18}FeO_3$ compound with the $PbZrO_3$-related $\sqrt{2}a_p \times 2\sqrt{2}a_p \times 4a_p$ perovskite-based structure and the *Pnam* space symmetry. The *Pnam* phase does not demonstrate a detectable homogeneity range. The IM phase is formed at $0.19 \le x \le 0.30$, and the *Pnma* $GdFeO_3$-type phase

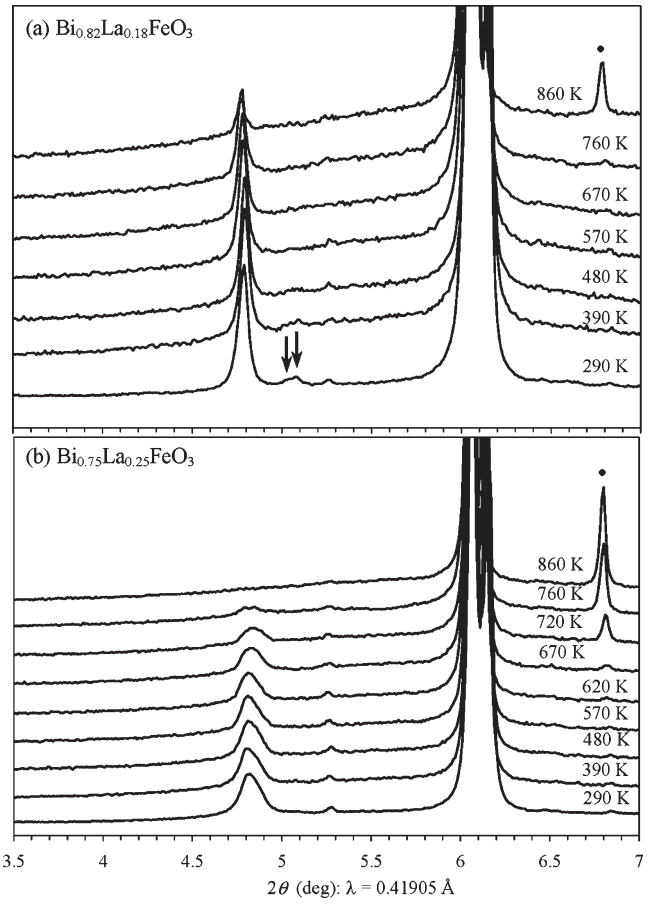

Figure 8. High-temperature synchrotron powder X-ray diffraction (HT SXRD) patterns of (a) $Bi_{0.82}La_{0.18}FeO_3$ and (b) $Bi_{0.75}La_{0.25}FeO_3$. (The solid circle symbol (●) represents a characteristic reflection of the $GdFeO_3$-type phase with space group *Pnma* ($\sqrt{2}a_p \times 2a_p \times \sqrt{2}a_p$). Arrows show superstructure reflections corresponding to $c = 4a_p$.)

($\sqrt{2}a_p \times 2a_p \times \sqrt{2}a_p$) is stable at $0.50 \le x \le 1$. A two-phase region was also observed in the $0.35 \le x \le 0.45$ range, separating the IM and *Pnma* phases.

Our results explain the controversy about the number of phases in the $(1-x)BiFeO_3-xLaFeO_3$ system. Note that the synthesis was often performed at 850−950 °C with short annealing times;[17,18,23−25] however, our results suggest that, at a temperature below 1000 °C, the equilibrium state cannot be reached in this system. During the synthesis, the end members (the $R3c$ and $GdFeO_3$-type phases) are formed first.[26] It seems that the properties have been measured on multiphased samples; in particular, the presence of the ferroelectric $R3c$ phase is a possible reason for the observation of ferroelectric properties up to $x = 0.4-0.5$.[15,18]

The most intriguing issue of the bulk $(1-x)$-$BiFeO_3-xLaFeO_3$ system is the presence of the IM structure. An overview of the $Bi_{0.75}La_{0.25}FeO_3$ structure is given in Figure 9. The primary modulation of the displacement of the Bi and O1 atoms is clearly visible. It is caused by a displacement of the Bi and O1 atoms along the *a*-axis toward each other. This local configuration is shown in Figure 10. These displacements occur along the $\langle 110 \rangle_p$ direction and have a polar character (i.e., create a local electric dipole, associated with the chain of the Bi and O1 atoms running along the *a*-axis). The dipoles associated with the chains mutually compensate each other, resulting in an antipolar structure. This compensation occurs mainly as intralayer ordering, where, within the $y = {}^1/_4$ or ${}^3/_4$ layer, the perfect antipolar $++--$ sequence of the Bi−O1 chains is only locally violated by insertion of a $+++$ or $---$ fragment (the plus and minus signs mark the relative direction of displacement of the chains). This creates a local uncompensated dipole moment in the ((Bi,La)O1) layer. The structure compensates this moment by adopting the opposite direction of chain displacement in the neighboring ((Bi,La)O1) layer, so that local fluctuations of the intralayer ordering are compensated by interaction with the neighboring layers. One can speculate that the displacement is caused by a localization of the lone pair on the Bi^{3+} cation. Such localization requires a strong covalent bonding between

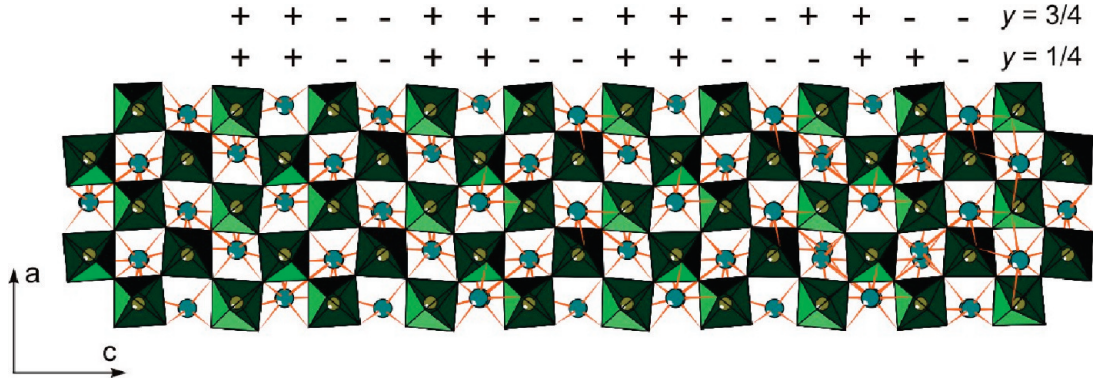

Figure 9. Overview of the $Bi_{0.75}La_{0.25}FeO_3$ crystal structure. The Bi atoms are shown as green spheres, the La atoms are not shown for clarity, and the Fe atoms are inside of the octahedra. The plus and minus signs mark the displacement directions of the Bi atoms in the Bi−O1 chains running along the *a*-axis. The in-phase displacement in the $y = {}^1/_4, {}^3/_4$ (BiO1) layers prevails in the structure. Note the antiphase displacements at the region where the $++--$ sequence is violated by the $---$ fragment.

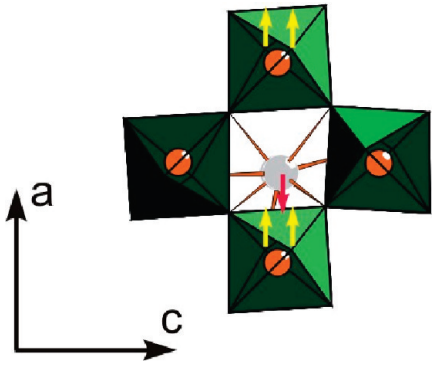

Figure 10. Local configuration in the $Bi_{0.75}La_{0.25}FeO_3$ crystal structure. The Bi atom is shown as a gray sphere, and the Fe atoms are shown as orange spheres. Oxygen atoms are located at the corners of octahedra. The displacements of the Bi and O1 atoms are marked with red and yellow arrows, respectively.

Bi and some oxygen atom; this bond is formed between Bi and O1 atoms, shortening the Bi−O1 interatomic distance. This can be considered as a driving force for the polar displacement. The secondary modulation occurs because of displacement of the O2 atoms within the *ac* plane. Locally, the result of this displacement can be considered as the a^+ octahedral tilt component added to the $a^0b^-b^-$ tilt system of the average *Imma* structure (the tilt notations are given according to ref 31). However, noticeable deformation of the FeO_6 octahedra also interleaves with the a^+ component: in the regions of the $+++$ or $---$ fragments, the tilt is becoming smaller and deformation prevails. It is possible that the driving force for the incommensurability is the coupling of the polar displacements and the a^+ octahedral tilt through the lattice strain, but the exact nature of this coupling can be clarified only if the displacement modulations of the O2 atom will be characterized with higher precision, which requires powder neutron diffraction data. The coupling between the displacements of the Bi−O1 chains and the a^+ octahedral tilt component is confirmed by the structural phase transition from the IM phase to the *Pnma* $GdFeO_3$-type phase upon heating. An ordered displacement of the Bi−O1 chains and the associated strain are suppressed by heating, and the $a^+b^-b^-$ tilt system is established, corresponding to the *Pnma* symmetry.

The IM phases have antipolar atomic displacements; however, this does not necessary mean that they should exhibit antiferroelectric properties similar to $PbZrO_3$. The same can be assumed for $Bi_{0.82}La_{0.18}FeO_3$ with the $PbZrO_3$-related structure. The electric field required for the observation of double polarization−electric field ($P-E$) hysteresis loops may be larger than the breakdown field. Some thin-film samples of $Bi_{1-x}Ln_xFeO_3$ (Ln = Sm, Gd, and Dy) show double $P-E$ hysteresis loops at certain Ln concentrations.[13] However, to the best of our knowledge, there are no such observations in bulk $Bi_{1-x}Ln_xFeO_3$ materials.

The isovalent substitution in $Bi_{1-x}Ln_xFeO_3$ (where Ln is a rare-earth element) is sometimes termed as the application of "chemical pressure" to $BiFeO_3$.[2] The $GdFeO_3$-type phase is stabilized at lower x for smaller Ln^{3+} ions. The smaller the Ln^{3+} ion, the narrower the stability ranges of other modifications. La^{3+} has almost the same ionic radius as Bi^{3+}. Therefore, the $Bi_{1-x}La_xFeO_3$ solid solutions exhibit the largest variety of structural modifications among $Bi_{1-x}Ln_xFeO_3$. It is interesting to note that the application of external pressure to undoped $BiFeO_3$ also produces more structural variations, including the $PbZrO_3$-type phase with the $\sqrt{2}a_p \times 2\sqrt{2}a_p \times 4a_p$ superstructure[32] and the $GdFeO_3$-type phase.[33] The stain effect in thin films is another parameter that can modify subtle phase relations in the $Bi_{1-x}La_xFeO_3$ system, resulting in shifts of phase boundaries and phase sequences.[34]

Acknowledgment. This work was supported by World Premier International Research Center Initiative (WPI Initiative, MEXT, Japan), the NIMS Individual-Type Competitive Research Grant, the Japan Society for the Promotion of Science (JSPS) through its "Funding Program for World-Leading Innovative R&D on Science and Technology (FIRST Program)", and the Grants-in-Aid for Scientific Research (22246083) from JSPS, Japan. The synchrotron radiation experiments were performed at the SPring-8 with the approval of the Japan Synchrotron Radiation Research Institute (under Proposal Nos. 2009A1136 and 2010A1215). We thank Dr. J. Kim and Dr. N. Tsuji for their assistance at SPring-8.

Supporting Information Available: Details of XRD patterns, derivation of the superspace model for the IM phase, temperature and compositional dependence of lattice parameters, crystal structure data of the *Pnma* phase, and magnetic and DSC data (PDF). This material is available free of charge via the Internet at http://pubs.acs.org.

(31) Howard, C. J.; Stokes, H. T. *Acta Crystallogr., Sect. B: Struct. Sci.* **1998**, *54*, 782.
(32) Belik, A. A.; Yusa, H.; Hirao, N.; Ohishi, Y.; Takayama-Muromachi, E. *Chem. Mater.* **2009**, *21*, 3400.
(33) Haumont, R.; Bouvier, P.; Pashkin, A.; Rabia, K.; Frank, S.; Dkhil, B.; Crichton, W. A.; Kuntscher, C. A.; Kreisel, J. *Phys. Rev. B* **2009**, *79*, 184110.
(34) Cheng, C. J.; Kan, D.; Anbusathaiah, V.; Takeuchi, I.; Nagarajan, V. *Appl. Phys. Lett.* **2010**, *97*, 212905.